Energy & Environmental Science

Accepted Manuscript

This is an *Accepted Manuscript*, which has been through the Royal Society of Chemistry peer review process and has been accepted for publication.

Accepted Manuscripts are published online shortly after acceptance, before technical editing, formatting and proof reading. Using this free service, authors can make their results available to the community, in citable form, before we publish the edited article. We will replace this *Accepted Manuscript* with the edited and formatted *Advance Article* as soon as it is available.

You can find more information about *Accepted Manuscripts* in the Information for Authors.

Please note that technical editing may introduce minor changes to the text and/or graphics, which may alter content. The journal's standard Terms & Conditions and the Ethical guidelines still apply. In no event shall the Royal Society of Chemistry be held responsible for any errors or omissions in this *Accepted Manuscript* or any consequences arising from the use of any information it contains.

ROYAL SOCIETY OF CHEMISTRY

www.rsc.org/ees

Deterministic Modelling of Carbon Nanotube Near-Infrared Solar Cells

Darin O. Bellisario[§], Rishabh M. Jain[£], Zackary Ulissi[‡], Michael S. Strano[†,‡]

[‡]Department of Chemical Engineering, Massachusetts Institute of Technology, Cambridge, Massachusetts 02139, USA.

[§]Department of Chemistry, Massachusetts Institute of Technology, Cambridge, Massachusetts 02139, USA.

[£]Department of Materials Science & Engineering, Massachusetts Institute of Technology, Cambridge, Massachusetts 02139, USA.

[†]Corresponding author: strano@mit.edu

Keywords: Single walled carbon nanotube, photovoltaic, solar cell, exciton, nanotechnology, renewable energy, carbon nanomaterials

Abstract

Photovoltaics (PVs) using single-walled carbon nanotubes (SWNTs) as near-infrared photo-absorbers have progressed rapidly, offering promise for long-wavelength light harvesting devices. Despite this interest the fundamental design questions remain, such as optimal device thickness, nanotube orientation, density, and the impact of impurities. To address this challenge, we develop a deterministic model of SWNT PVs derived directly from SWNT photophysics using photon, exciton, and charge carrier population balances. The model accounts for arbitrary distributions of nanotube chiralities, lengths, orientations, defect types and concentrations, bundle fraction and size, and density. We show that feasible devices can achieve external quantum efficiencies above 60%. We reveal a sharply optimal device

Energy & Environmental Science Accepted Manuscript

thickness that is a function of nanotube density, orientation, and quenching site concentration. This thickness stems from a tradeoff between exciton generation and diffusion to the electrodes, and is at a minimum at the limit of close-packed nanotube density. We show that this minimum characterizes a given device design and scales with mean nanotube length to exponent 0.4. The normalized difference between optimal thickness and this close-packed limit scales inversely with density to the 0.24 power. Practically, in-plane aligned nanotube configurations yield optimal thicknesses less than 10 nm, increasing to a range of 50 to 200 nm for vertical alignment. Due to weak inter-SWNT exciton transport relative to exceptional intra-SWNT diffusion, vertically-aligned films are unambiguously favored at densities above 3% of the close-packed limit; at lower densities however an optimum emerges at an intermediate angle to compensate for weaker light absorption of vertical nanotubes. Comparison to published experimental devices displays the model's utility for device design.

Energy & Environmental Science Accepted Manuscript

Introduction

Both cost and performance requirements make semiconducting single-walled carbon nanotubes (SWNT) attractive as photo-absorbers for near-infrared photovoltaic (nIR PV) applications.[1-7] Their solution-process-ability (which can substantially reduce manufacturing costs), earth-abundant source materials, and recently scale-able fabrication and purification may yield low cost manufacture, a limitation with conventional solar cell (SC) designs.[3, 5, 6, 8-10] Furthermore, such devices can augment the photo-conversion efficiencies of conventional visible-PV systems by absorbing nIR wavelengths that comprise approximately 22% of the solar spectrum but fall within a typical PV bandgap. Here, low unit-operations costs particularly enable this application by making stacked independent PV layers (four-terminal SCs) feasible, versus the constraints of one-step fabrication (*i.e.* lattice, bandgap, and workfunction matching constraints) that have challenged tandem multi-junction (two-terminal) SCs.[11] SWNT are also attractive relative to many other organic and inorganic PV materials through exceptional exciton and free carrier diffusivity and mobility, exceptional absorption cross-sections, and resistance to oxidation by water and oxygen.[3, 5, 6, 12-15] To date, single-walled nanotube (SWNT) SCs with 0.01-1.7% external quantum efficiency (EQE) have been developed employing single chiralities,[2, 4] mixed semiconducting chiralities,[1, 3] and mixed semiconducting and metal chiralities[5, 6] in bulk heterojunction[3, 7] and planar heterojunction[1, 2, 4] configurations using polymers[16] and fullerenes[1-4] for exciton dissociation and/or co-photoabsorption. Despite this progress, even the most basic questions of suitable device properties, such as nanotube chirality, density, orientation, film thickness, *etc.*, remain unanswered; there is currently no model describing steady-state SWNT PV operation for the selection of design variables. There are even conflicting proposals for optimal nanotube orientation.[6] As with any nanostructured optoelectronics, complex dynamics and a huge space of design variables stymie both empirical studies and simple intuition. In this work, we address this gap by developing the first deterministic model of carbon nanotube photovoltaics. By analogy, we can note the impact that quasi-fermi-level transport models and the depletion zone approximation describing bulk semiconductor p-n junction PVs have had on cell design.[17]

Energy & Environmental Science Accepted Manuscript

The model, a set of integro-differential equations, is derived directly from the fundamental physics of SWNT light-matter interaction, exciton transport, and free carrier transport. We achieved this by adopting an approximation of macroscopic ($O(100\,nm)$) homogeneity. This allowed us to treat relevant local (single-SWNT) properties as random variables, describing the network of nanotubes as a distribution of those properties. We focus on planar heterojunction devices. Our method applies to arbitrary networks in terms of chemical and structural properties – *e.g.* any distribution of nanotube chiralities, lengths, orientations, defect types and levels, bundle fraction and size, density, dielectric environment, or electrode combination. Rigorously, it is limited to densities above the percolation threshold, although it is quantitatively consistent with recent observations at lower densities in the literature.

We apply the model to elucidate the optimal device design as a function of nanotube orientation, packing density, defect density, and nanotube length. An optimal film thickness, T^*, emerges that decreases with density, impurity concentration, and in-plane alignment component to balance light absorption with exciton diffusion length and exciton-electrode separation. We find that such devices are characterized by a minimum optimal thickness, T^*_{CP}, at close-packed density ρ_{CP}. Devices at lower nanotube densities have optimal thicknesses T^* that scale with the normalized difference $T^* - T^*_{CP}$; we capture that trend analytically with two constants. We also show that T^*_{CP} has a scaling with mean nanotube length to the 0.4 power.

Nanotube alignment angle (*e.g.* vertical, horizontal) balances much faster intra- versus inter-nanotube exciton diffusion with higher axial versus radial absorptivity. At sufficiently high densities (above 3% of close-packed) vertically aligned films are shown to be unambiguously favored to maximize exciton transport, but as density is lowered to below 10% of close-packed a second optimum emerges for some thicknesses at an intermediate angle – $\pi/3$ to $\pi/4$ from the vertical axis – to compensate for the decreasing light absorption. Of all film properties, density and alignment are most important in determining efficiency, with 10- to 100-fold performance improvements achieved through vertical

Energy & Environmental Science Accepted Manuscript

alignment and increasing density above 10% of close-packed ($O(10^{17}\ m/m^3)$ length of SWNT per volume). The implications of these predictions are that next generation devices should focus on higher densities and vertical alignment, and thicknesses in the range of 40-100 nm depending on their other properties.

Model

For brevity only a summary of the derivation is produced here; a full derivation is presented in the Supporting Information (SI). We consider a network of single-walled nanotubes (SWNT) sandwiched between two electrode semi-infinite plates separated by a distance T (Figure 1). We define a Cartesian z axis in the propagation direction of the incident solar photon flux $J_0(\omega)$ at $z = 0$. The back electrode has reflectance $0 \leq R \leq 1$ which can in general be frequency dependent. A variety of conduction and valence band charge collecting electrode (type II exciton dissociation interface) configurations are possible, including those where an electrode also acts as a photoabsorbing layer (*e.g.* fullerenes[1, 2, 7]). We focus on the relatively general case of two dissociating electrodes, but the model applies generally.

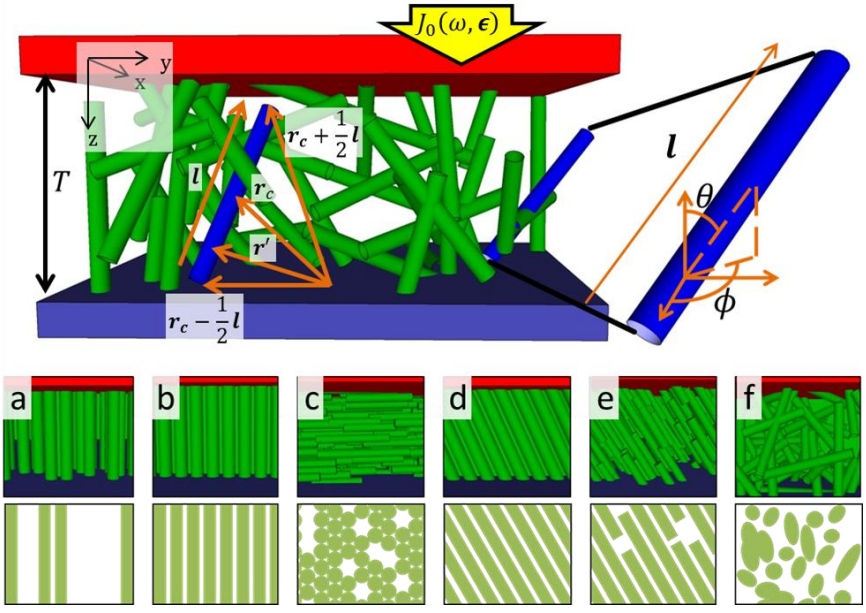

Figure 1. Cartoon of model geometry, depicting the position $\boldsymbol{r_c}$, orientation $\hat{\boldsymbol{l}} \equiv (\theta, \phi)$, and length l of nanotubes. The thickness of the film is T, and we take the z axis to be the propagation direction of incident irradiance $J_0(\omega, \boldsymbol{\epsilon})$. A point on a given tube is

Energy & Environmental Science Accepted Manuscript

$\boldsymbol{r}'$. (a-f) Cartoon representations of film geometries under consideration, side view (top) and cross-section (bottom). Vertically aligned films with densities ranging from sparse (a) to close-packed (b), horizontally aligned films at densities above the percolation threshold (c), aligned films at arbitrary angles with single-layer (d) and multi-layer (e) depositions (see text, SI), and isotropic films (f).

We define an individual nanotube in our network, which we approximate as a rigid rod, as a set of parameters: position, length, orientation, and chirality.[18] In the global coordinate system the center of each nanotube is located at $\boldsymbol{r}_c$ relative to an arbitrary origin in the xy plane at $z = 0$. The length l and orientation $\hat{\boldsymbol{l}} \equiv (\theta, \phi)$ of the tube form a spherical-coordinate vector $\boldsymbol{l} = (l, \theta, \phi)$. The ends of a single SWNT are therefore located, relative to the origin, at the ends of vectors $\boldsymbol{r}_c \pm \frac{1}{2}\boldsymbol{l}$. A point $\boldsymbol{r}'$ along the central axis of the SWNT is then confined to the line segment between the ends. In describing intra-SWNT mechanics we will also consider the one-dimensional space along a nanotube axis, denoting that coordinate $r_l = \alpha_l l,\ \alpha_l \in [0,1]$. A nanotube also has a chirality $\boldsymbol{c} \equiv (n_1, n_2)$ where n_1 and n_2 are chiral indices.[19] For convenience we index all chiralities present in the network by integer i (chirality $\boldsymbol{c}_i$) in order of increasing exciton (optical) band gap $E_{i+1} > E_i$. Each chirality has an associated center-center diameter $d_{\boldsymbol{c},c-c}$, and an outer diameter $d_{\boldsymbol{c}}$.

The properties $\{\boldsymbol{r}_C, \boldsymbol{l}, \boldsymbol{c}\}$ completely define a given nanotube in our network. Our approach begins with treating these parameters as random variables, defining a given film by their distributions:

$$
\begin{aligned}
& p(\boldsymbol{r}_C|\boldsymbol{r}) = p\left(r_{cx}, r_{cy}, r_{cz}\middle|\boldsymbol{r}\right) \\
& p(\boldsymbol{l}) = p(l) \cdot p(\theta, \phi) \\
& p(\boldsymbol{c}_i) = v_i \in [0,1], \qquad \sum_i v_i = 1
\end{aligned}
\tag{1}
$$

where v_i is the number fraction of chirality i in the film. Our derivation is general for cases where any of these properties vary systematically with depth, *i.e.* $p(\boldsymbol{r}_C, \boldsymbol{l}, \boldsymbol{c}|z)$, or are correlated with one another, but in most practical applications $p(\boldsymbol{l})$ and $p(\boldsymbol{c}_i)$ are spatially invariant and the variables are independent.

Solving the steady state operation of the illuminated film breaks into three distinct problems: light interaction, exciton transport, and free carrier transport. Beginning with treatment of the light field, At

Energy & Environmental Science Accepted Manuscript

any given point $\boldsymbol{r} = (x, y, z)$ there is a total photon flux $J_v(\boldsymbol{r})$ that is distributed over (as $J_v(\omega, \boldsymbol{\epsilon}, \boldsymbol{k}|\boldsymbol{r})$; *i.e.* irradiance) frequency ω, linear polarization component $\boldsymbol{\epsilon} = (\theta_\epsilon, \phi_\epsilon)$, and propagation direction $\boldsymbol{k} = (\theta_k, \phi_k)$.

To a first approximation we treat absorption as the only light-matter interaction under consideration in the film, neglecting the weaker mechanisms of elastic scattering and photoluminescence (PL); see SI for discussion and justification. To treat attenuation of the field we derive the polarization- and frequency-dependent absorption cross-section of the film from the single-SWNT absorption behavior. By considering the dipole approximation in a perturbation theory treatment of light-matter interaction, we arrive at the absorption cross-section for a single nanotube of orientation $\hat{\boldsymbol{l}} = (\theta, \phi)$,

$$\sigma(\boldsymbol{c}_i, \boldsymbol{\epsilon}, \hat{\boldsymbol{l}}, \omega) = \left|\boldsymbol{\epsilon} \cdot \hat{\boldsymbol{l}}\right|^2 \sigma_{\parallel}(\boldsymbol{c}_i, \omega) + \left(1 - \left|\boldsymbol{\epsilon} \cdot \hat{\boldsymbol{l}}\right|\right)^2 \sigma_{\perp}(\boldsymbol{c}_i, \omega), \quad (2)$$

where $\sigma_{\parallel}$ and $\sigma_{\perp}$ are the absorption cross-sections for light polarized parallel and perpendicular, respectively, to the SWNT longitudinal axis, reflecting the two anisotropic sets of optically active electronic transitions.[20] Over all frequencies, the parallel absorption cross section is on average approximately six times greater than the perpendicular one due to depolarization effects.[20] For later convenience we normalize the cross-section to per-unit-length, σ_l, rather than the more common per-carbon. Over our length-scales of interest ($< 1\ \mu m$) for SWNT material, we neglect phase shifts such as refraction that introduce circular polarization components to the light field.

From the perspective of the gradient in the light field, the diameter of the SWNT is negligible and the film is essentially homogenous (see SI). For irradiance $J_v(\omega, \boldsymbol{\epsilon}, \boldsymbol{k}|\boldsymbol{r})$ the photon absorption rate per volume due to SWNT of chirality i oriented in $\hat{\boldsymbol{l}}$ are

$$N_i(\omega, \boldsymbol{\epsilon}, \boldsymbol{k}, \hat{\boldsymbol{l}}|\boldsymbol{r}) = v_i \cdot \rho_{\langle l \rangle} \cdot \sigma_l(\boldsymbol{\epsilon}, \hat{\boldsymbol{l}}, \omega, \boldsymbol{c}_i) \cdot J_v(\omega, \boldsymbol{\epsilon}, \boldsymbol{k}|\boldsymbol{r}) \quad (3)$$

where $\rho_{\langle l \rangle} = \rho \cdot \langle l \rangle$ is the length-normalized SWNT film density (ρ is the number density, $\langle l \rangle$ is the mean nanotube length). To get the total film absorption rate we must sum absorption terms (3) for nanotubes at each possible orientation $\hat{\boldsymbol{l}}$ and chirality i, weighted by the relative populations of each. That is equivalent

Energy & Environmental Science Accepted Manuscript

however to integrating over the distribution $p(\hat{\boldsymbol{l}})$ (and summing over chiralities), forming the crux of our methodology,

$$N(\omega, \boldsymbol{\epsilon}, \boldsymbol{k}|\boldsymbol{r}) = \sum_i \int_0^{2\pi} p(\phi) \int_0^{\pi} p(\theta)\, N_i\left(\omega, \boldsymbol{\epsilon}, \boldsymbol{k}, \hat{\boldsymbol{l}}|\boldsymbol{r}\right) d\theta\, d\phi. \tag{4}$$

In this manner, we can describe the light interaction behavior of the film by integrating the single-SWNT behavior over the distribution of independent single-SWNT properties; we will take the same approach to exciton and free carrier transport below.

A steady-state balance on the light intensity yields

$$\nabla \cdot J_v(\omega, \boldsymbol{\epsilon}, \boldsymbol{k}|\boldsymbol{r}) = -N(\omega, \boldsymbol{\epsilon}, \boldsymbol{k}|\boldsymbol{r}). \tag{5}$$

Two useful reductions then emerge. First, neglecting Rayleigh scattering and photoluminescence the $\boldsymbol{k}$ dependence drops out. Second, in the x and y dimensions where our film is infinite we take periodic solutions as trivial, making our boundary conditions in those dimensions uniformity, *i.e.*

$$\frac{dJ_v}{dy} = 0, \qquad \frac{dJ_v}{dx} = 0. \tag{6}$$

Our balance then simplifies to

$$\frac{dJ_v(\omega, \boldsymbol{\epsilon}|z)}{dz} = -\sum_i N_i(\omega, \boldsymbol{\epsilon}|z). \tag{7}$$

The linear differential equation (7) can be solved for a transparent back electrode subject to the boundary condition of perpendicularly incident light unpolarized in the xy plane,

$$J_v(\omega, \boldsymbol{\epsilon}|z = 0) = J_0(\omega, \boldsymbol{\epsilon}) = J_0(\omega) \cdot \delta\left(\theta_\epsilon - \frac{\pi}{2}\right) \cdot \frac{1}{2\pi}, \qquad \phi_{\boldsymbol{\epsilon}} \in [0, 2\pi]. \tag{8}$$

We treat reflection off the back electrode without the propagation vector $\boldsymbol{k}$ by breaking the light field into approximately non-interfering 'forward' and 'reverse' fluxes $J_F(\omega, \boldsymbol{\epsilon}|z)$ and $J_R(\omega, \boldsymbol{\epsilon}|z)$ (See SI), where the boundary condition of the latter is the reflection of the former at $z = T$.

In SWNT, optical electronic excitations result in exciton generation – bound carrier states – rather than free charges, due to one dimensional confinement resulting in a weak dielectric environment.[21-24] To

Energy & Environmental Science Accepted Manuscript

collect charges in a solar cell, excitons must be dissociated either at a type II interface or by an electric field imparting coulomb force greater than the binding energy. Examining the relevant physical quantities (see SI), we validate the approximation that nonradiative decay of hot excitons to the band gap is essentially instantaneous over our length scales of interest. This simplification allows us to treat the exciton generation rate at band gap energy E_i as the total photon absorption rate at all energies $\hbar\omega > E_i$ for chirality i, $N_i(z)$.

A single empirical diffusion coefficient describing exciton transport in a film would be limited to only a particular geometry and chemistry. Instead, we start with the intra-tube 1D exciton reaction-diffusion behavior, then deriving the contribution of a network of such systems to three-dimensional exciton transport, and finally coupling nanotubes via exciton hopping (EH), sometimes termed exciton energy transfer.

Along a single nanotube axis there is an exciton concentration profile $n(r_l)$. We construct a steady-state exciton population balance along r_l including the generation rate $N(r_l) = N(\boldsymbol{r}')$, longitudinal diffusion, and relaxation due to localized impurities, exciton-exciton annihilation (EEA), radiative decay, and end-quenching. This yields the steady-state differential equation (see SI)

$$\frac{dn}{dt} = N(r_l) + D_l\frac{d^2n}{dr_l^2} - k_\Gamma n - k_{EEA}n^2 - \sum_{im} k_{im}n_{im}n - k_{end}\big(\delta(r_l - 0) + \delta(r_l - l)\big)n = 0, \quad (9)$$

where D_l is the longitudinal diffusion coefficient, k_Γ, k_{EEA}, k_{im}, and k_{end} are, respectively, the radiative, EEA, impurity (of type im, *e.g.*, oxidative agents, catalyst nanoparticles), and end-quenching rate constants, and n_{im} is the number of impurity contacts per length of SWNT.

To determine the network behavior, we construct a three dimensional population balance subject to diffusion in one dimensional channels. Starting with a single chirality, the diffusion flux (not yet including SWNT-SWNT interactions) due to nanotubes of orientation $\hat{\boldsymbol{l}}$ is

Energy & Environmental Science Accepted Manuscript

(10) $$D_l(\sin\theta\cos\phi)^2\frac{\partial c}{\partial x} + D_l(\sin\theta\sin\phi)^2\frac{\partial c}{\partial y} + D_l(\cos\theta)^2\frac{\partial c}{\partial z}$$

where $c(\boldsymbol{r})$ is the 3D exciton density. This expression is arrived at by considering 1D channels penetrating the faces of a differential volume (see SI). Note that while Equation (10) has the form of what one would empirically intuit, there is the crucial difference that D_l is exactly the single-SWNT exciton diffusion coefficient, not a net film coefficient.

Next we extend film relaxation kinetics to 3D. We multiply the reaction rates per length of SWNT by $\rho_{\langle l\rangle}$ to convert to rate per volume network under an assumption of macroscopic homogeneity (see SI). The resulting quenching terms are

(11) $$-k_\Gamma c - k_{im}n_{im}c - \frac{k_{EEA}}{\rho_{\langle l\rangle}}c^2 - \frac{k_{end}}{\rho_{\langle l\rangle}}c_{end}(\boldsymbol{r})\cdot c,$$

where $c_{end}(\boldsymbol{r}) = p(\boldsymbol{r}_{end} = \boldsymbol{r}_C \pm \boldsymbol{l}|\boldsymbol{r})$ is the distribution of nanotube ends in the film (see SI). Note the value of our treatment in that all of $\{k_{im}, k_{EEA}, k_{end}\}$ are single-nanotube 1D rate constants, deducible experimentally or theoretically from individual SWNT physics.

Finally we consider exciton transport between nanotubes. The mechanisms of exciton transfer/hopping (EH) between nanotubes of the same and different chirality, as well as the mechanisms of type II exciton dissociation at donor-acceptor interfaces, remain under investigation and debate.[1, 3, 25-27] Explicitly, in the model we treat EH as a tunneling process in bundles and at interconnects, neglecting admittedly vital phenomena such as exciton delocalization[26, 28] and Schottky barriers/band bending.[27, 29] As those physics are discovered, the new functional forms can be seamlessly introduced into our model using the same independent parameters.

We divide the film into two distinct microscopic environments: bundles and interconnects. The bundling coefficient, b_c, we define as the length fraction of SWNT in bundles. Along with the mean number of SWNT in a bundle, M_b, we determine the diffusion coefficient in a bundle orthogonal to the longitudinal axis (see SI),

Energy & Environmental Science Accepted Manuscript

(12) $$D_{EH,b} = \chi \frac{1}{4} k_{EH,b} (\Delta_B + d_c)^2,$$

where $\chi(M_b)$ is the mean number of nearest neighbors, Δ_B is the inter-SWNT separation in a bundle, and $k_{EH,b}$ is the elastic exciton transition rate. Beginning with a monochiral film, this yields a film exciton flux due to bundling,

(13) $$b_c(1 - \sin\theta\cos\phi)^2 D_{EH,b} \frac{\partial c}{\partial x} + b_c(1 - \sin\theta\sin\phi)^2 D_{EH,b} \frac{\partial c}{\partial y} + b_c(1 - \cos\theta)^2 D_{EH,b} \frac{\partial c}{\partial z}.$$

At interconnects, we consider the number of intersections per length of a nanotube in a control volume around a nanotube,

(14) $$n_I = \left(1 - b_c\left(1 - \frac{1}{M_B}\right)\right) \rho \frac{15}{4} \pi d_c^2.$$

That yields a film exciton flux (still for a monochiral film),

(15) $$Let\ \gamma_I \equiv \left(1 - b_c\left(1 - \frac{1}{M_B}\right)\right) d_c \cdot n_I = \rho \left(1 - b_c\left(1 - \frac{1}{M_B}\right)\right)^2 \frac{15}{4} \pi d_c^3$$
$$(1 - \sin\theta\cos\phi)^2 \cdot \gamma_I \cdot D_{EH,I} \frac{\partial c}{\partial x} + (1 - \sin\theta\sin\phi)^2 \cdot \gamma_I \cdot D_{EH,I} \frac{\partial c}{\partial y} + (1 - \cos\theta)^2 \cdot \gamma_I \cdot D_{EH,I} \frac{\partial c}{\partial z},$$

where the orthogonal diffusivity at interconnects is

(16) $$D_{EH,I} = \frac{1}{2} k_{EH,I} \lambda^2 (\Delta_I + d_c)^2,$$

where Δ_I is the inter-SWNT separation at contacts, $k_{EH,I}$ is the elastic transition rate, and λ is the co-alignment:

(17) $$\lambda \equiv \left|\hat{\boldsymbol{l}}' \cdot \hat{\boldsymbol{l}}''\right| = \lambda(\theta', \theta'', \phi', \phi''),$$

for an arbitrary pair of nanotubes, with a distribution extractable from $p(\hat{\boldsymbol{l}})$ (see SI).

Energy & Environmental Science Accepted Manuscript

Including all three diffusion mechanisms, we then have the volume balance for exciton transport in a monochiral network. We simplify that expression by again recognizing that periodic solutions in the xy plane are trivial for our purposes, reducing our steady state problem to a differential equation in z,

$$Let \quad D_{tot} \equiv (\cos\theta)^2 D_l + (1-\cos\theta)^2\left(\gamma_I D_{EH,I} + b_c D_{EH,b}\right)$$

$$\frac{dc}{dt} = N(z) + D_{tot}\frac{d^2c}{dz^2} - k_\Gamma c - c\sum_{im} k_{im} n_{im} - \frac{k_{EEA}}{\rho_{\langle l\rangle}}c^2 - \frac{k_{end}}{\rho_{\langle l\rangle}} c_{end}(z)\cdot c. \tag{18}$$

Analogous to the light absorption problem, we have constructed a differential equation describing exciton transport due to nanotubes with orientation $\hat{\boldsymbol{l}}$, but to get the total balance we must sum contributions from all possible orientations. Again, that weighted sum is equivalent to integrating (18) over the distribution $p(\hat{\boldsymbol{l}})$. This treatment is only valid under our approximation of a homogenous film (see SI). That summarizes our method: treat single-nanotube chemical and geometric properties as random variables, derive the network behavior for given values of those parameters, and finally integrate the solution over their distribution. In the *Results* section we illustrate this process when we apply it to specific cases.

Note that equation (18) has an intuitive reaction-diffusion form, but A) the net diffusivity D_{tot} and several of the kinetic rate constants depend on the film properties ($p(\hat{\boldsymbol{l}}), \rho_{\langle l\rangle}, p(l)$), and B) by considering the distributions of single-SWNT parameters and the microscopic mechanisms of exciton transport and decay, we have been able to derive the dependence of network diffusion and reaction constants on film properties and fundamental single-exciton physical constants.

Multiple chiralities, including metallic SWNT (mSWNT), which quench excitons through rapid nonradiative decay, are then introduced. We construct volume balances for each chirality i analogous to the monochiral balance (18), but with additional quenching terms due to EH to mSWNT in bundles and at interconnects, and pairwise coupling terms to one another due to EH to lower-bandgap chiralities. This yields a system of ordinary differential equations:

Energy & Environmental Science Accepted Manuscript

$$\frac{dc_i}{dt} = v_i N(z) + D_{tot}\frac{d^2c_i}{dz^2} - k_\Gamma c_i - c_i\sum_{im} k_{im}n_{im} - \frac{k_{EEA}}{\rho_{\langle l\rangle}}c_i^2$$
$$- \frac{k_{end}}{\rho_{\langle l\rangle}}c_{end}(z)\cdot c_i - k_{EH}\langle\lambda^2\rangle\cdot v_m\gamma_I c_i$$
$$- b_c D_{EH,b} v_m \frac{2}{\sqrt{3}} d_{\boldsymbol{c}}^{-2}\cdot c_i$$
$$- c_i\sum_{j<i}\left(k_{EH}\langle\lambda^2\rangle\cdot v_j\gamma_I + b_c\cdot D_{EH,b}v_j\frac{2}{\sqrt{3}}d_{\boldsymbol{c}}^{-2}\right)$$
$$+ \sum_{j>i} c_j\cdot\left(k_{EH}\langle\lambda^2\rangle\cdot v_j\gamma_I + b_c\cdot D_{EH,b}v_j\frac{2}{\sqrt{3}}d_{\boldsymbol{c}}^{-2}\right), \quad (19)$$

where v_m is the fraction of mSWNT in the film, and again we have indexed the chiralities as monotonically increasing in optical band gap ($E_{i+1} > E_i$).

The system of ODEs (19) can be integrated over the relevant distributions and solved at steady state subject to boundary conditions at the electrodes ($z = 0, T$). A variety of electrode configurations can be considered; here we focus on two electrodes that can drive type II exciton dissociation – one hole accepting and one electron accepting. For each electrode we therefore have Robin boundary conditions from the exciton splitting rate,

$$\left.\frac{dc_i}{dz}\right|_{z=0} = \frac{k_{d0,i}}{D_{tot}}c_i(z=0)$$
$$\left.\frac{dc_i}{dz}\right|_{z=T} = -\frac{k_{dT,i}}{D_{tot}}c_i(z=T). \quad (20)$$

where $k_{d0,i}$ and $k_{dT,i}$ are the dissociation rate constants that in general could depend on the chirality i.

We add to the model the drift-diffusion transport of charge carriers resulting from exciton dissociation. In addition to the analogous geometric effects on film charge mobility and diffusivity, charge transfer at the interface of nanotubes, particularly of different chiralities, can block or trap charges.[29] Asymmetric electron and hole generation (at the two electrodes) can lead to an electric field development that feeds back on the exciton dissociation problem, inhibiting dissociation and/or driving

Energy & Environmental Science Accepted Manuscript

spontaneous in-film dissociation when the field strength exceeds the binding energy. Finally carrier densities can significantly impact mobility.[30]

In this work we do not seek to accurately describe free carrier transport in the SWNT film. Rather, we proceed under the simplification that performance will be limited by exciton diffusion, due to high longitudinal mobilities in any intrinsic electric field.[30] This assumption reduces coupling between the free carrier and exciton problems to the exciton dissociation rate. We also continue to neglect any charge-transfer effects at inter-SWNT contacts, as those effects have been neither theoretically nor experimentally quantified. These rough assumptions allow, as we show, important results in the optimization of film performance, but prohibit accurate quantitative prediction of external quantum efficiency (EQE). In future work, we will seek to develop a more complete consideration of free carrier transport.

As an estimate, we attenuate single-SWNT electron and hole mobilities, μ_e^* and μ_h^*, by the network attenuation of single-SWNT exciton diffusivities. We then balance the non-equilibrium populations of conduction band carriers, $f_e(\boldsymbol{r})$, and valence band carriers, $f_h(\boldsymbol{r})$, which are coupled to one another and the electric field $\mathcal{E}_z(z)$. This yields population balances

$$\frac{df_e}{dt} = 0 = D_e \frac{d^2 f_e}{dx} + \mu_e \left(\mathcal{E}_z \frac{df_e}{dx} + f_e \frac{d\mathcal{E}_z}{dx} \right) - k_{e-h} f_e f_h. \tag{21}$$

$$\frac{df_h}{dt} = 0 = D_h \frac{d^2 f_h}{dx} - \mu_h \left(\mathcal{E}_z \frac{df_h}{dx} + f_h \frac{d\mathcal{E}_z}{dx} \right) - k_{e-h} f_e f_h, \tag{22}$$

where $D_{e/h}$ and $\mu_{e/h}$ are the conduction/valence band carrier network diffusivity and mobility, respectively, and k_{e-h} is the electron-hole recombination rate constant. Equations (21) and (22) are subject to generation boundary conditions from exciton dissociation at one electrode, and a Robin (reaction) boundary condition due to extraction at the opposite electrode (see SI). The electric field evolves in the z axis from the gradient in excess charge populations,

$$\frac{d\mathcal{E}_z}{dz} = \frac{q}{\varepsilon} \big(f_h(z) - f_e(z) \big), \tag{23}$$

Energy & Environmental Science Accepted Manuscript

where ε is the mean permittivity of the film. The intrinsic bias across the film from mismatched electrode work function forms the boundary condition to (23).

Parameter Estimation

We apply the model to monochiral (6,5) films with both isotropic (see SI) and aligned orientation distributions (Figure 1). Relevant physical constants are determined from experimental measurement or through estimation (see SI). We took the intensity and frequency distribution of incident light to be the AM1.5 solar spectrum, which we fit by subtracting Gaussian curves from a blackbody spectrum. For the absorption cross-sections $\sigma_{\parallel}(\omega)$ and $\sigma_{\perp}(\omega)$ we normalized the absorption spectrum of a solid (6,5) film[2] to the (6,5) absorption cross-section at S_{22} measured from single SWNT in reference [31]. We estimate exciton and free carrier diffusivity and quenching rate constants by analyzing the body of literature (see SI).

Model Solution for Aligned Film

We assume a SWNT length distribution as log-normal[32] We begin with mean length $\langle l \rangle = 400\ nm$ and second moment $20^2\ nm^2$. The fixed angle of alignment relative to the z axis we define as θ', and we focus on the case of perfect alignment,

(24) $$p(\theta) = \delta(\theta - \theta'), \qquad \theta' \in \left[0, \frac{\pi}{2}\right].$$

In the xy plane all angles are equivalent in our semi-infinite film; we choose orientation along the x axis,

(25) $$p(\phi) = \delta(\phi - 0).$$

The film thickness, T, we will vary, but it can be limited by deposition morphology: if the aligned film is grown or stacked in a single 'forest' or 'layer' (Figure 1d), T cannot exceed the height in z of that single layer, $\langle l \rangle \cos\theta'$; additionally the distribution of $c_{end}(z)$ will be heterogenous (log-normal). If instead the film is 'sliced' out of a network mixed in all dimensions, like a typical solution-processed

Energy & Environmental Science Accepted Manuscript

horizontally aligned film,[33] (Figure 1e) any thickness is hypothetically permissible, and $c_{end} = 2\rho$ is homogenous. These two film types and our handling of them are discussed in the SI.

Beginning our calculation with the irradiance, the absorption cross-section polarization dependence is described as equation (2) for our single chirality. We are in a position now to evaluate the dot product, $\boldsymbol{\epsilon} \cdot \hat{\boldsymbol{l}}$, by integrating the photon balance over $p(\hat{\boldsymbol{l}})$ (equation (33)). That yields the absorption cross-section (see SI)

$$\sigma_l(\boldsymbol{\epsilon}, \omega) = \sigma_{l,meas}(\omega)\left(\frac{5}{6}(\sin\theta_\epsilon \cos\phi_\epsilon \sin\theta' + \cos\theta_\epsilon \cos\theta')^2 + \frac{1}{6}(1 - |\sin\theta_\epsilon \cos\phi_\epsilon \sin\theta' - \cos\theta_\epsilon \cos\theta'|)^2\right). \tag{26}$$

Solving the photon balance (7) with no z dependence to $\rho_{\langle l \rangle}$ or σ_l, subject to the incident unpolarized solar flux boundary condition (8), and integrating over $\theta_{\boldsymbol{\epsilon}}$, our forward flux becomes (see SI),

$$J_F(\omega, \phi_\epsilon | z) = \frac{1}{2\pi} J_0(\omega) \cdot \exp\left[-\rho_{\langle l \rangle}\sigma_{l,meas}(\omega)\left(\frac{5}{6}(\cos\phi_\epsilon \sin\theta')^2 + \frac{1}{6}(1 - |\cos\phi_\epsilon \sin\theta'|)^2\right) z\right]. \tag{27}$$

Note that except in the vertically-aligned case ($\theta' = 0$), there is an xy-plane linear polarization dependence to the field absorption. With a boundary condition of reflectance R off the back electrode we solve the reverse flux differential equation, again substituting in $\sigma_l(\boldsymbol{\epsilon}, \omega)$ and integrating over θ_ϵ to yield

$$J_R(\omega, \phi_\epsilon | z) = \frac{1}{2\pi} \cdot R \cdot J_0(\omega) \cdot \exp\left[-\rho_{\langle l \rangle}\sigma_{l,meas}(\omega)\left(\frac{5}{6}(\cos\phi_\epsilon \sin\theta')^2 + \frac{1}{6}(1 - |\cos\phi_\epsilon \sin\theta'|)^2\right) \cdot (2T - z)\right]. \tag{28}$$

The total light field gradient would then be

$$J_v(\omega, \phi_\epsilon | z) = J_R(\omega, \phi_\epsilon | z) + J_F(\omega, \phi_\epsilon | z), \tag{29}$$

for example plotted in Figure 2 for horizontally and vertically aligned films.

The exciton generation rate is the light absorption rate integrated over frequency and polarity,

Energy & Environmental Science Accepted Manuscript

(30) $$N(z) = \int_0^{2\pi} \int_0^{\infty} \rho_{\langle l \rangle} J_v(\omega, \phi_\epsilon | z) \sigma_l(\phi_\epsilon, \omega) \; d\omega d\phi_\epsilon.$$

We then resolve the monochiral exciton balance (18) with the physical constants estimated in the SI. With an aligned film, our macroscopic homogeneity approximation limits the density space we can probe; for films with an in-plane (horizontal) orientation component, our treatment of exciton hopping is valid only at densities above the percolation threshold ($\rho/\rho_{CP} > 0.65$ for a horizontally-aligned film $\theta' = \pi/2$).[34] Otherwise, we would be erroneously assuming in our orthogonal diffusion coefficient that percolation pathways uniformly exist. Above the threshold, we safely have a uniform orthogonal diffusivity ($\gamma_I \to 0$). Integrating the balance (18) over $p(\hat{\boldsymbol{l}})$ ((24) and (25)), the net diffusion coefficient reduces to

(31) $$D_{tot} = D_l(\cos\theta')^2 + (1 - \cos\theta')^2 D_{EH,b}.$$

With $\Delta_B \ll d_{\boldsymbol{c}}$, Equation (12) yields $D_{EH,b} = 1.8 \times 10^{-7}\ m^2/s$; note this diffusivity is 5 orders of magnitude lower than D_l ($\cong 10^{-2}\ m^2/s$, see SI). We then numerically solve (18) at steady state, subject to electrode boundary conditions (20).

Aligned Film Results

We can first compare the two extreme cases, vertically ($\theta' = 0$) and horizontally ($\theta' = \pi/2$) aligned, at the same density, thickness, *etc.* ($T = 40\ nm$, $\rho_{\langle l \rangle} = 0.8\rho_{\langle l \rangle}^{CP}$, $R = 1$, $\langle l \rangle = 800\ nm$, no added impurities; Figure 2). The vertical forest presents the incident light with only the perpendicular absorption cross-section (axial transition dipole), while the horizontal film can be excited along both the longitudinal and the axial transition dipoles, leading to anisotropic absorption (Figure 2b). The higher parallel absorption cross-section makes a substantial difference in total absorptivity even at this high density and with the aligned-film diminishing returns of more rapidly depleting parallel-polarized irradiance (Figure 2b). For these particular vertical and horizontal films, the total absorbances are 1.51 and 2.13 respectively. In absolute intensity absorption of visible light is higher than nIR (Figure 2a) due to greater visible irradiance in the incident solar flux, but normalized for intensity nIR absorption is greater (Figure 2d). As

Energy & Environmental Science Accepted Manuscript

light travels through the film, the anisotropy of the horizontal network induces a linear polarization (Figure 2b).

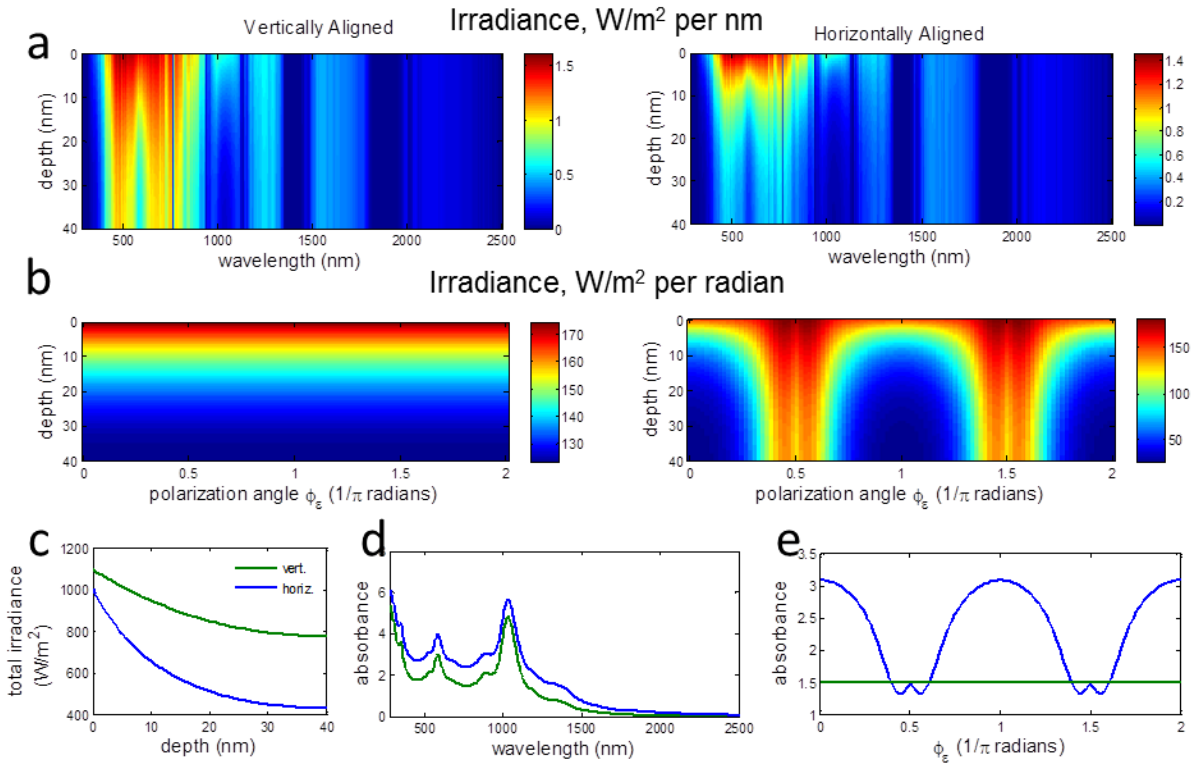

Figure 2. Comparison of vertically (green, $\theta' = 0$) and horizontally (blue, $\theta' = \pi/2$) aligned films at $T = 40\ nm$, $\rho_{\langle l \rangle} = 0.8\rho_{\langle l \rangle}^{CP}$, $R = 1$. a) irradiance per wavelength as light travels through the film. Note the more rapid attenuation in the horizontally aligned case. b) irradiance per linear polarization angle in the xy-plane as light travels through the film, showing the isotropic absorption of the vertically aligned film and induced linear polarization in the horizontally-aligned film. c) total irradiance with depth in the film, integrated over all wavelengths and polarization angles. d) total film absorbance as a function of wavelength. e) total film absorbance as a function of polarization angle. For exciton concentration gradients and the relative impact of each quenching mechanism, see SI.

Despite the higher absorbance, the substantially lower diffusivity in the charge-collecting axis of the horizontally aligned film ($D_{tot} = O(10^{-2}\ m^2/s)$ versus $O(10^{-7}\ m^2/s)$) greatly limits the efficiency – for these films EQEs are 64.6% and 2.7% respectively for vertically and horizontally aligned. In the horizontally aligned case a diffusion length of less than 10 nm is observed (see SI), consistent with experimental findings.[1] With current experimental techniques however, horizontally aligned films can be

Energy & Environmental Science Accepted Manuscript

made with substantially higher densities than vertically aligned films, which presently are grown as forests.[2, 35-37] To evaluate the impact of this limitation, we explored the density-thickness space at the two orientations.

Considering an idealized case where the nanotubes are infinitely long and there are no impurities of any kind (Figure 3),[38] one observes that performance is not monotonically increasing in the amount of light absorbed. Rather at a given density there is an optimal thickness that shifts lower with higher density (also observed in the case of finite length, see Figure 4c). This result reflects the well-known trade-off with increasing thickness between greater total exciton generation (more light absorption) but greater mean distance a generated exciton has to travel to reach an electrode.[39] The same tradeoff is reflected in the much lower optimal thickness of horizontal compared to vertical films; as noted, the diffusivity in the charge-collecting axis is several orders of magnitude lower in the horizontal film, leading to a diffusion length of order 10 nm. As a result, above a few tens of nanometers there are diminishing returns to greater absorption due to low exciton collection, consistent with recent experimental realization of higher performance in order-10-nm essentially-horizontal films versus previous order-100-nm films.[4] In contrast, vertically aligned films, where exciton dissociation is driven in the axis parallel to longitudinal diffusion, shows optimal thicknesses two orders of magnitude larger than horizontal films. The enormous longitudinal SWNT diffusion coefficient further manifests as substantially higher performance of vertically aligned films versus horizontally aligned films above 1%CP density. The higher absorptivity of the horizontally aligned film (due primarily to depolarization) is not sufficient to compensate for the difference in diffusivity except at very low thicknesses and densities. In both cases, as density rises the optimal thickness shifts lower: higher density increases the light absorbed per thickness, shifting the optimum more towards favoring exciton transport (Figure 4).

Energy & Environmental Science Accepted Manuscript

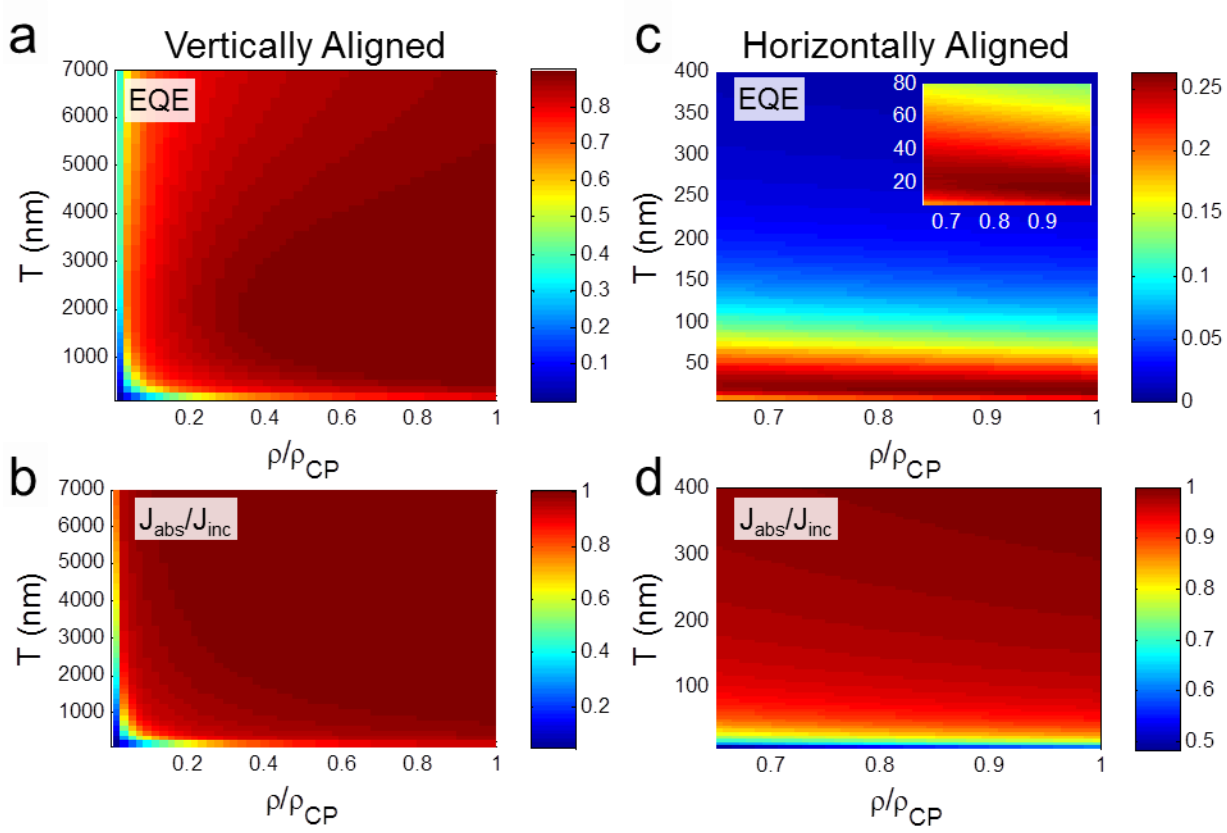

Figure 3. External quantum efficiency (EQE) (a,c) and total fraction of incident light absorbed (b,d) versus nanotube density (ρ/ρ_{CP}) and device thickness (T) for horizontally and vertically aligned films with infinitely long tubes and no impurities. For horizontal films, we look only at the density space above the percolation threshold (see text). $R = 1$.

We then examined the effect of introducing finite nanotube length to the network, permitting end-quenching of excitons (Figure 4). We observed that not only does EQE across the parametric space drop (as we would expect), but that the lower exciton diffusion length has the effect of shifting the optimal thickness from the absorption-diffusion tradeoff lower, compressing the density-thickness trend in the T axis. At a fixed density, shorter tubes reduce the optimal thickness (Figure 4c). This trend is analogous to the inverse relationship of density and optimal thickness: as exciton transport weakens (in this case due to quenching) relative to light absorption (exciton generation), the balance shifts to increase exciton diffusion by reducing the thickness.

Energy & Environmental Science Accepted Manuscript

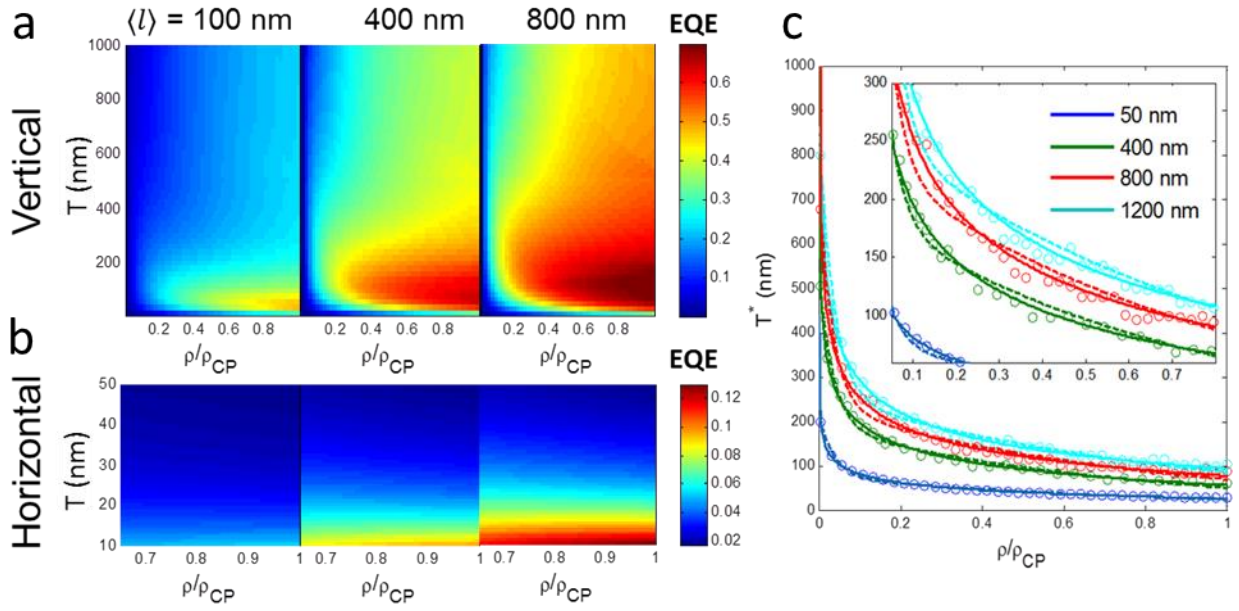

Figure 4. EQE versus thickness T and density for vertically- (a) and horizontally- (b) aligned films at different mean nanotube lengths (100, 400, and 800 nm). See SI for single-curve visualization of these calculations showing shift in optimal thickness. (c) Trend of optimal thickness T^* with density at different fixed mean lengths ($\langle l \rangle$ = 50, 400, 800, and 1200 nm) for vertically-aligned films. Circles are numerical result, solid lines are power law fits and dashed lines are biexponential fit (see text). Numerical results exhibit noise because of low sensitivity ($O(10\,nm)$) of EQE to thickness close to the optimum. Inset: zoom showing the 'cusp' where $dT^*/d\rho$ rapidly lowers and the biexponential trend is least accurate. See SI for fit parameters, more curves, plots of maximum efficiency (at T^*) versus $\langle l \rangle$, EQE versus T at varying fixed densities illustrating the optimality-shift, and comparison of the exciton concentration gradients.

Remarkably, the trends in T^* with density are exactly captured by a power law relationship (Figure 4c), with the power coefficients themselves inversely proportional to quenching site concentration (proportional to $\langle l \rangle$) (see SI).

We find that the optimal film thickness at maximum density ($\rho/\rho_{CP} \to 1$), T^*_{CP}, is an important length scale for the device. T^*_{CP} depends on quenching site concentration, with lower $\langle l \rangle$ yielding lower optimal thickness due to reduced diffusion length, following a strict power law trend (Figure 5 inset, SI):

$$T^*_{CP}(\langle l \rangle) = 52\ nm^{0.6} \cdot \langle l \rangle^{0.4}. \quad (32)$$

Energy & Environmental Science Accepted Manuscript

Using this minimal device thickness, one finds that an appropriate dimensionless thickness for the device emerges as $(T^* - T^*_{CP})/T^*_{CP}$, which collapses all of the density versus thickness trends to a single curve (Figure 5). The trend is described as a power law in normalized nanotube density:

$$\frac{T^* - T^*_{CP}(\langle l \rangle)}{T^*_{CP}(\langle l \rangle)} = a\left[\left(\frac{\rho}{\rho_{CP}}\right)^b - 1\right]. \quad (33)$$

The values we get for the dimensionless coefficients, which are invariant with quenching site concentration, are $a = 2.7 \pm 0.1$ and $b = -0.241 \pm 0.005$. In this way, equation (33) should find utility in device design as a single analytic equation describing the optimal device thickness as a function of density and quenching site concentration (32). We suspect that this tool will find utility among experimentalists, who can use it to calculate the optimal device thickness, which is one of the more feasible design parameters to control, given a film density and nanotube length (which can also be measured and controlled).

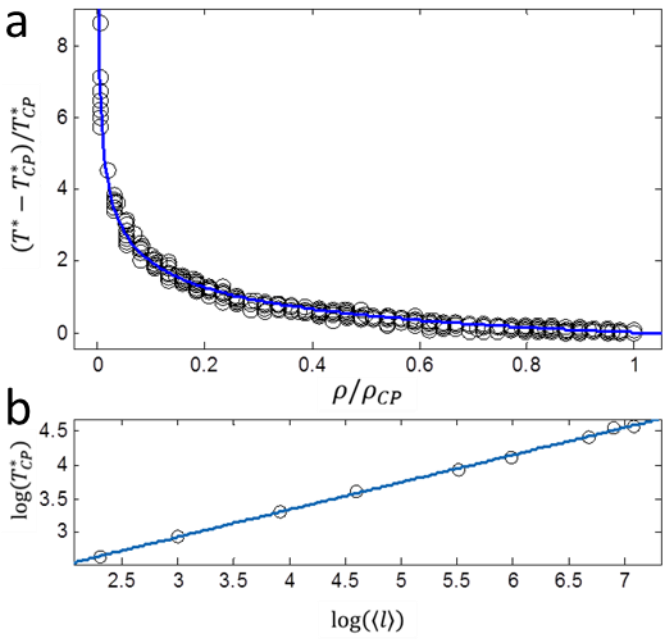

Figure 5. (a) Trend of optimal thickness numerical results with density, plotted relative to optimal thickness at close-packed density (see text). The data (black circles) includes results from devices with $\langle l \rangle = 10, 20, 50, 100, 250, 400, 800, 1000$, and $1200\ nm$, showing that on this plot they all collapse to a single trend. The blue curve is a fit of equation (33), showing perfect

Energy & Environmental Science Accepted Manuscript

agreement (well within numerical result variation). (b) the trend of the optimal thickness at close-packed density (T_{CP}^{*}) with mean nanotube length (inverse impurity concentration) on a log-log scale, showing that they exhibt a strict power law relationship.

Next we introduced impurity scattering of excitons, providing varying concentrations of a generic local impurity that rapidly quenches excitons, choosing a representative $\langle l \rangle = 400\ nm$ (Figure 6). The same trend as end quenching emerged, with higher impurity concentrations lowering the diffusion length and both decreasing the mean performance and compressing the trend it in the T dimension.

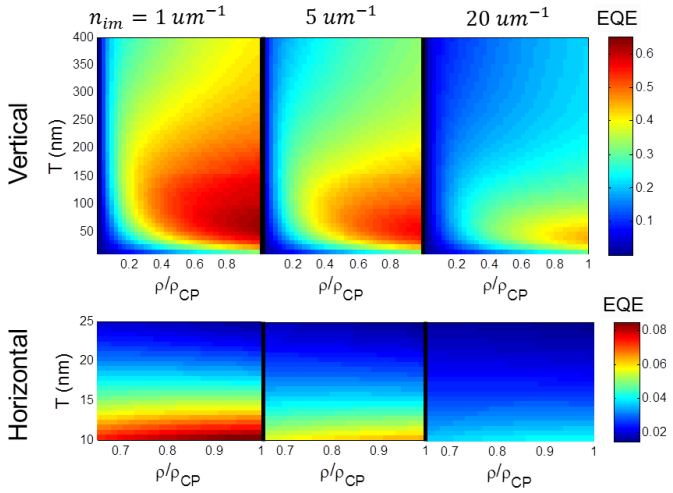

Figure 6. Efficiency versus thickness and density for vertically and horizontally aligned films with $\langle l \rangle = 400\ nm$ at different local quenching impurity concentrations (1, 5, and 20 per micron).

Understanding that thickness and density play critical roles, we turned to examining the alignment angle choice. At a given density we look at the thickness-angle space (Figure 7). Below 10%CP density, two local thickness-angle optima emerge, one at the extreme of vertical alignment, and the other at an intermediary angle. As thickness increases, the optimal alignment angle shifts gradually towards more vertical, compensating for the increased mean exciton-electrode separation with a higher z-diffusion coefficient (larger longitudinal intra-SWNT diffusion component, lower orthogonal inter-SWNT); also as thickness rises, the ratio of vertical performance to intermediate performance shifts towards vertical. As density rises, the intermediate peak more rapidly converges to the vertical with increasing T, and the ratio becomes more favorable across all T to vertical alignment. As a result, at low density (<3%CP) the intermediate peak is the global optimum of performance, while at high density the

Energy & Environmental Science Accepted Manuscript

vertical is superior. In absolute efficiency, we again observe the strong impact of density (note scale bars in Figure 7), particularly at lower densities. Again we can consider experimental results, and note that as existing SWNT SC devices have been made with primarily nanotubes in the xy plane at low concentrations (<1% CP density), the observed EQEs from 0.1% to 1% are quantitatively consistent with our predictions.[1-4] Our results suggest that developing vertically aligned films above 10% the close-packed density would yield substantial EQE improvements. Films with high in-plane components, such as most to-date devices, are the worst possible configurations of nanotubes.

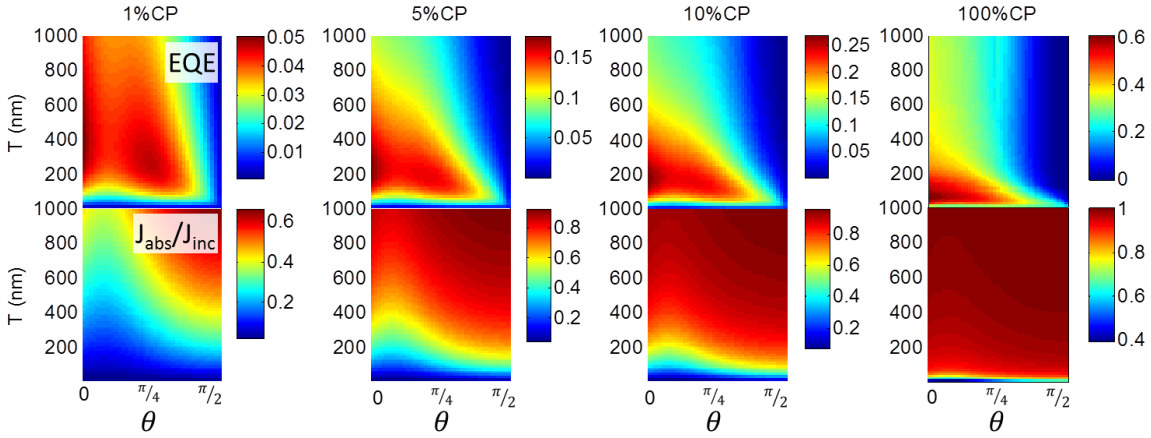

Figure 7. Performance and fraction of light absorbed versus device thickness T and aligned film nanotube orientation θ at 1%, 5%, 10%, and 100% close-packed density. $\theta = 0$ is a vertical film, $\theta = \pi/2$ is a horizontal film. $\langle l \rangle = 400\ nm, n_{im} = 2 \times 10^6\ m^{-1}, R = 1$.

The optimal orientation results can be interpreted again by understanding the balance of light absorption and exciton diffusion constraints. Vertical alignment provides more rapid diffusion via the longitudinal SWNT axis, but absorbance is lower due to the depolarization effect. Horizontal alignment comes at the cost of much slower exciton-transfer-dependent diffusion, but provides more rapid light absorption, which to some extent mitigates the diffusion constraints by generating more excitons closer to the top electrode. Longitudinal diffusivity, $O(10^{-2}\ m^2/s)$, is so much greater than orthogonal diffusivity, $O(10^{-7} m^2/s)$, that in all but nearly-horizontal films it dominates the net diffusion coefficient. Because of the rapid exciton transport longitudinally between electrodes, absorptivity increases from somewhat non-vertical alignment at lower densities yield efficiency gains. Those gains are highest at low T where

Energy & Environmental Science Accepted Manuscript

absorption is weakest and diminish (shifting the intermediate peak more vertical) with increasing thickness. At sufficiently high densities the absorption gains are unnecessary, leading to a global vertical-growth optimum. In general, the aligned film limits light absorption off of the parallel axis (Figure 2e), reducing the efficacy of alignment.

Comparison to To-Date Experimental Results

With these results we were able to consider the differences among to-date experimental SWNT SC observations. More closely examining the vertically- and horizontally-aligned film density trends (Figure 6), we see that at low densities (<10%CP, where all devices have been) the increase in performance with density is rapid (Figure 3, Figure 6);[40] higher density increases absorption without decreasing the diffusion length (neglecting coherent delocalization of excitons between tubes, see *limitations* section), leading to substantial performance gains at low density. Comparison to currently published SWNT photovoltaics[1-4] suggests 1) that experimentally observed EQE variations may be due to relatively low densities, and 2) that large gains can be realized in performance with higher density films. The caveat is a need to be reasonably close ($0.5T^* < T < 3T^*$) to the high-performance thickness regime. For example in primarily in-plane ('horizontal') films where the *z* diffusion length is short, density gains are negligible if the thickness is already limiting generated exciton collection significantly. With reasonable length and impurity terms, this is consistent with T^* below 15 nm for horizontally aligned films, explaining the improvements in performance by reducing thickness in reference 4. In general, the existence of a thickness optimum has been experimentally observed in both planar[1] and bulk[7] heterojunctions, albeit at densities below our cutoff of robust validity.

Model Limitations

Several explicit and implicit approximations have been made in the derivation of the model. To encourage both application of the model and its further development, we would like to discuss some of the most significant limitations.

Energy & Environmental Science Accepted Manuscript

In both the exciton and free carrier transport problems, we neglect equilibrium charge transfer at the interface of nanotubes, particularly those of different chirality; in reality, Schottky barriers/band bending likely occurs at these contacts,[29] which can greatly alter inter-SWNT transport. We expect this phenomenon to play a substantial role in free carrier transport in particular, which is one reason we adopted a simplified model of steady state charge distribution (See SI). Presently, experimental or theoretical examinations are necessary to elucidate the energetic and spatial character of the effect. A more accurate model should account for these interfacial interactions and local electric fields in the inter-SWNT coupling terms. Along the same lines, we have neglected the possibility of coherent delocalization of excitons in bundles, which recent experiments suggest to be the case;[26] this effect could substantially raise orthogonal exciton diffusion lengths in bundles.

We have also neglected Rayleigh scattering and photoluminescence processes in the light-matter interaction. These assumptions simplified our application of the model tremendously (see SI), at the potential cost of accuracy. See the SI for a discussion of the implications of this approximation.

Finally, the validity of our integration over single-SWNT properties rests on an approximation of homogeneity. This limitation has significant implications for certain cases, particularly in-plane ('horizontally') aligned, low-density films. The conditions and implications of this error, including estimation of the impact, are discussed in depth in the SI section '*Macroscopic Heterogeneity.*' The homogeneity approximation also implies that we can only treat cases with SWNT densities above the percolation threshold.[34]

Conclusions

In conclusion, we have developed a deterministic model of a nIR absorbing single walled carbon nanotube photovoltaic cell based on exciton population balances that include generation, transport, recombination and charge separation. Available model inputs include arbitrary distributions of nanotube chiralities, lengths, orientations, defect types and concentration, bundle fraction and size, density, dielectric environment, and electrode combination. Several important findings include that a minimal,

Energy & Environmental Science Accepted Manuscript

optimal thickness corresponding to the close packing limit of nanotubes at zero free volume provides an important scaling for the device thickness. This value is shown to scale with average nanotube length to the power 0.4. At lower densities, the normalized difference between optimal thickness and the close-packed limit scales inversely with density to the 0.24 power. Practically, the horizontally (in-plane) aligned nanotube configurations yield optimal thicknesses less than 10 nm but increase to a range of 50 to 200 nm for vertical alignment. Due to weak inter-SWNT exciton transport relative to exceptional intra-SWNT diffusion, vertically-aligned films are unambiguously favored at densities above 3% of the close-packed limit; at lower densities however an optimum emerges at an intermediate angle to compensate for weaker light absorption of vertical nanotubes. Despite the recent focus on horizontal alignment, we show that for solar energy applications horizontal alignment is the worst possible configuration. In depositing films for example, even adding inert features such as polystyrene beads to increase the out-of-plane component of nanotubes could improve performance despite the reduction in density. Based on these results we conclude that next generation devices should include higher densities and target vertical alignment, with thicknesses in the range of 40-100 nm depending on density, average SWNT length and estimated defect density.

Acknowledgements

DOB and RMJ were supported by the Department of Defense through the National Defense Science and Engineering Graduate Fellowship Program. RMJ also acknowledges support through the NSF Graduate Research Fellowship Program.

Electronic Supplementary Information (SI) available: The supporting information contains a full derivation of the model, as well as analysis of several its tangential aspects, along with a table of variables. Notes on physical constant estimation and more results of the model application are also provided, as indicated above. See DOI: 10.1039/b000000x/

Energy & Environmental Science Accepted Manuscript

References

1. Bindl, D. J.; Shea, M. J.; Arnold, M. S., Enhancing extraction of photogenerated excitons from semiconducting carbon nanotube films as photocurrent. *Chem Phys* **2013,** *413*, 29-34.
2. Jain, R. M.; Howden, R.; Tvrdy, K.; Shimizu, S.; Hilmer, A. J.; McNicholas, T. P.; Gleason, K. K.; Strano, M. S., Polymer-Free Near-Infrared Photovoltaics with Single Chirality (6,5) Semiconducting Carbon Nanotube Active Layers. *Adv Mater* **2012,** *24* (32), 4436-4439.
3. Bernardi, M.; Lohrman, J.; Kumar, P. V.; Kirkeminde, A.; Ferralis, N.; Grossman, J. C.; Ren, S. Q., Nanocarbon-Based Photovoltaics. *Acs Nano* **2012,** *6* (10), 8896-8903.
4. Shea, M. J.; Arnold, M. S., 1% solar cells derived from ultrathin carbon nanotube photoabsorbing films. *Applied Physics Letters* **2013,** *102* (24), 243101.
5. Wang, L.; Liu, H.; Konik, R. M.; Misewich, J. A.; Wong, S. S., Carbon nanotube-based heterostructures for solar energy applications. *Chemical Society Reviews* **2013,** *42* (20), 8134-8156.
6. Arnold, M. S.; Blackburn, J.; Crochet, J.; Doorn, S.; Duque, J.; Mohite, A.; Telg, H., Recent Developments in the Photophysics of Single-Wall Carbon Nanotubes for Active and Passive Material Elements in Thin Film Photovoltaics. *Physical Chemistry Chemical Physics* **2013**.
7. Ye, Y.; Bindl, D. J.; Jacobberger, R. M.; Wu, M.-Y.; Roy, S. S.; Arnold, M. S., Semiconducting Carbon Nanotube Aerogel Bulk Heterojunction Solar Cells. *Small* **2014**, n/a-n/a.
8. Liu, H.; Nishide, D.; Tanaka, T.; Kataura, H., Large-scale single-chirality separation of single-wall carbon nanotubes by simple gel chromatography. *Nat Commun* **2011,** *2*, 309.
9. Tvrdy, K.; Jain, R. M.; Han, R.; Hilmer, A. J.; McNicholas, T. P.; Strano, M. S., A Kinetic Model for the Deterministic Prediction of Gel-Based Single-Chirality Single-Walled Carbon Nanotube Separation. *Acs Nano* **2013,** *7* (2), 1779-1789.
10. Moshammer, K.; Hennrich, F.; Kappes, M., Selective suspension in aqueous sodium dodecyl sulfate according to electronic structure type allows simple separation of metallic from semiconducting single-walled carbon nanotubes. *Nano Res.* **2009,** *2* (8), 599-606.
11. Brown, A. S.; Green, M. A., Limiting efficiency for current-constrained two-terminal tandem cell stacks. *Progress in Photovoltaics: Research and Applications* **2002,** *10* (5), 299-307.
12. Schoppler, F.; Mann, C.; Hain, T. C.; Neubauer, F. M.; Privitera, G.; Bonaccorso, F.; Chu, D. P.; Ferrari, A. C.; Hertel, T., Molar Extinction Coefficient of Single-Wall Carbon Nanotubes. *J Phys Chem C* **2011,** *115* (30), 14682-14686.
13. Naumov, A. V.; Tsyboulski, D. A.; Bachilo, S. M.; Weisman, R. B., Length-dependent optical properties of single-walled carbon nanotube samples. *Chem Phys* (0).
14. Ruzicka, B. A.; Wang, R.; Lohrman, J.; Ren, S. Q.; Zhao, H., Exciton diffusion in semiconducting single-walled carbon nanotubes studied by transient absorption microscopy. *Phys Rev B* **2012,** *86* (20).
15. Gabor, N. M.; Zhong, Z. H.; Bosnick, K.; McEuen, P. L., Ultrafast Photocurrent Measurement of the Escape Time of Electrons and Holes from Carbon Nanotube p-i-n Photodiodes. *Phys Rev Lett* **2012,** *108* (8).
16. Ren, S. Q.; Bernardi, M.; Lunt, R. R.; Bulovic, V.; Grossman, J. C.; Gradecak, S., Toward Efficient Carbon Nanotube/P3HT Solar Cells: Active Layer Morphology, Electrical, and Optical Properties. *Nano Lett* **2011,** *11* (12), 5316-5321.
17. Nelson, J., *The physics of solar cells*. Imperial College Press: London, 2003; p xix, 363 p.
18. More parameters can be introduced into the model in the same manner as we include these; see SI.
19. Reich, S.; Thomsen, C.; Maultzsch, J., *Carbon nanotubes : basic concepts and physical properties*. Wiley-VCH: Weinheim ; Cambridge, 2004; p ix, 215 p.
20. Islam, M. F.; Milkie, D. E.; Kane, C. L.; Yodh, A. G.; Kikkawa, J. M., Direct measurement of the polarized optical absorption cross section of single-wall carbon nanotubes. *Phys Rev Lett* **2004,** *93* (3).

Energy & Environmental Science Accepted Manuscript

21. Wang, F.; Dukovic, G.; Brus, L. E.; Heinz, T. F., The optical resonances in carbon nanotubes arise from excitons. *Science* **2005,** *308* (5723), 838-841.
22. Maultzsch, J.; Pomraenke, R.; Reich, S.; Chang, E.; Prezzi, D.; Ruini, A.; Molinari, E.; Strano, M. S.; Thomsen, C.; Lienau, C., Exciton binding energies in carbon nanotubes from two-photon photoluminescence. *Phys Rev B* **2005,** *72* (24).
23. Dukovic, G.; Wang, F.; Song, D. H.; Sfeir, M. Y.; Heinz, T. F.; Brus, L. E., Structural dependence of excitonic optical transitions and band-gap energies in carbon nanotubes. *Nano Lett* **2005,** *5* (11), 2314-2318.
24. Avouris, P.; Freitag, M.; Perebeinos, V., Carbon-nanotube photonics and optoelectronics. *Nat Photonics* **2008,** *2* (6), 341-350.
25. Luer, L.; Crochet, J.; Hertel, T.; Cerullo, G.; Lanzani, G., Ultrafast Excitation Energy Transfer in Small Semiconducting Carbon Nanotube Aggregates. *Acs Nano* **2010,** *4* (7), 4265-4273.
26. Crochet, J. J.; Sau, J. D.; Duque, J. G.; Doorn, S. K.; Cohen, M. L., Electrodynamic and Excitonic Intertube Interactions in Semiconducting Carbon Nanotube Aggregates. *Acs Nano* **2011,** *5* (4), 2611-2618.
27. Zhou, X.; Zifer, T.; Wong, B. M.; Krafcik, K. L.; Léonard, F.; Vance, A. L., Color Detection Using Chromophore-Nanotube Hybrid Devices. *Nano Letters* **2009,** *9* (3), 1028-1033.
28. Delaney, P.; Choi, H. J.; Ihm, J.; Louie, S. G.; Cohen, M. L., Broken symmetry and pseudogaps in ropes of carbon nanotubes. *Nature* **1998,** *391* (6666), 466-468.
29. Topinka, M. A.; Rowell, M. W.; Goldhaber-Gordon, D.; McGehee, M. D.; Hecht, D. S.; Gruner, G., Charge Transport in Interpenetrating Networks of Semiconducting and Metallic Carbon Nanotubes. *Nano Lett* **2009,** *9* (5), 1866-1871.
30. Yang, Z.; Liao, A.; Pop, E., Multiband Mobility in Semiconducting Carbon Nanotubes. *Electron Device Letters, IEEE* **2009,** *30* (10), 1078-1080.
31. Oudjedi, L.; Parra-Vasquez, A. N. G.; Godin, A. G.; Cognet, L.; Lounis, B., Metrological Investigation of the (6,5) Carbon Nanotube Absorption Cross Section. *The Journal of Physical Chemistry Letters* **2013,** *4* (9), 1460-1464.
32. Wang, S.; Liang, Z.; Wang, B.; Zhang, C., Statistical characterization of single-wall carbon nanotube length distribution. *Nanotechnology* **2006,** *17* (3), 634.
33. Sun, X.; Chen, T.; Yang, Z.; Peng, H., The Alignment of Carbon Nanotubes: An Effective Route To Extend Their Excellent Properties to Macroscopic Scale. *Accounts of Chemical Research* **2012,** *46* (2), 539-549.
34. Maillaud, L.; Zakri, C.; Ly, I.; Pénicaud, A.; Poulin, P., Conductivity of transparent electrodes made from interacting nanotubes. *Applied Physics Letters* **2013,** *103* (26), -.
35. Nessim, G. D.; Hart, A. J.; Kim, J. S.; Acquaviva, D.; Oh, J.; Morgan, C. D.; Seita, M.; Leib, J. S.; Thompson, C. V., Tuning of Vertically-Aligned Carbon Nanotube Diameter and Areal Density through Catalyst Pre-Treatment. *Nano Lett* **2008,** *8* (11), 3587-3593.
36. Fischer, J. E.; Zhou, W.; Vavro, J.; Llaguno, M. C.; Guthy, C.; Haggenmueller, R.; Casavant, M. J.; Walters, D. E.; Smalley, R. E., Magnetically aligned single wall carbon nanotube films: Preferred orientation and anisotropic transport properties. *J Appl Phys* **2003,** *93* (4), 2157-2163.
37. Lu, M.; Jang, M.-W.; Haugstad, G.; Campbell, S. A.; Cui, T., Well-aligned and suspended single-walled carbon nanotube film: Directed self-assembly, patterning, and characterization. *Applied Physics Letters* **2009,** *94* (26), 261903-3.
38. Note that while we do extract EQE, given the estimation of many parameters and the approximate consideration of charge transport we are not fixated on the absolute values of EQE; while they may be representative they are not fundamental, and are primarily valuable for comparing the differential impact of geometric and chemical parameters.

Energy & Environmental Science Accepted Manuscript

39. Wu, M. Y.; Jacobberger, R. M.; Arnold, M. S., Design length scales for carbon nanotube photoabsorber based photovoltaic materials and devices. *J Appl Phys* **2013,** *113* (20).

40. To observe this effect in horizontal films, we must go below the percolation threshold, which is not shown here. Quantitatively our predictions in that regime match up with experimental devices, but because our approximation does not hold in that regime, we do not claim to reproduce that device performance.

Energy & Environmental Science Accepted Manuscript

We investigate the optimal design of carbon nanotube near-IR solar cells, revealing a narrow density, thickness, and nanotube orientation space of maximum efficiency.

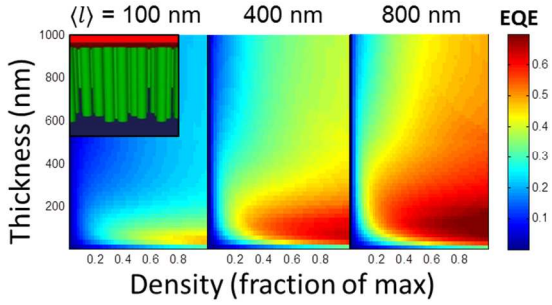

Energy & Environmental Science Accepted Manuscript